



# Experimental studies of Regulated Metal Deposition (RMD™) on ASTM A387 (11) steel: study of parametric influence and welding performance optimization

Dinbandhu<sup>1</sup> · Vishalkumar Prajapati<sup>1</sup> · Jay. J. Vora<sup>2</sup> · Subhash Das<sup>2,3</sup> · Kumar Abhishek<sup>1</sup>

Received: 16 April 2019 / Accepted: 18 December 2019 / Published online: 2 January 2020  
© The Brazilian Society of Mechanical Sciences and Engineering 2020

## Abstract

The present study aims to highlight the effect of the governing variables in regulated metal deposition (RMD™) on the mechanical properties and weld quality of low alloy steel. Current, voltage, and gas flow rate have been considered as main (RMD™) parameters, whereas heat-affected zone, depth of penetration, bead width, and bead height have been taken into account as welding performance characteristics. Signal to noise has been utilized in order to determine the optimal welding parameters, while analysis concerning the significant level of determination has been assessed using analysis of variance. Furthermore, the exploration of principal component analysis and combined quality loss concept integrated with the Taguchi method has been introduced to assess the favorable welding condition. The optimal favorable machine combination has been obtained as current = 100 A, V = 13 V, and gas flow rate = 21 L/min using both the methods.

**Keywords** Advanced GMAW · Regulated Metal Deposition (RMD™) · Principal component analysis · Combined quality loss

## 1 Introduction

Gas metal arc welding (GMAW), also known as metal inert gas welding (MIG) [1], is a process of joining metals by heating them to their melting points with an electric arc. Figure 1 demonstrates a general circuit diagram of the GMAW process. In it, a welding gun is used to feed a continuous consumable solid wire electrode into the weld pool and the two base materials being welded. To protect the weld pool from contamination, a shielding gas is also passed through

the welding gun [1, 2]. Figure 2 illustrates an enlarged view of the welding area.

Generally, the GMAW process can be performed in three ways, namely semiautomatic welding, machine welding, and automatic welding [2]. In semiautomatic GMAW, the movement of the welding gun is controlled by a human operator, whereas the equipment controls only the feeding of the electrode wire. Due to this, it is also known as handheld welding. But, in machine GMAW, the welding gun is connected to a manipulator. Instead of direct human interference, an operator sets and adjusts the controls for the movement of the manipulator. Automatic GMAW is a process that requires only occasional or no observation of welding, and no manual adjustments of the equipment controls [2, 7, 8].

Short circuit, globular, and spray arc transfers are the three modes of metal transfer in a GMAW process. These modes are the function of various weld parameters, namely arc current, arc voltage, type of shielding gas, and wire electrode feed speed and its diameter [2, 9]. The arc welding processes are dynamic in nature, and with conventional technologies and techniques, the controlling of aforesaid variables is extremely problematic [9]. Excessive spatter, porosity, lack of fusion, excessive penetration, warping, burn through, and weld puddle agitation are the most common

---

Technical Editor: Adriano Fagali de Souza.

---

✉ Kumar Abhishek  
krabhishek1987@gmail.com

<sup>1</sup> Department of Mechanical Engineering, Institute of Infrastructure Technology Research and Management (IITRAM), Ahmedabad, Gujarat 380026, India

<sup>2</sup> Department of Mechanical Engineering, School of Technology, Pandit Deendayal Petroleum University, Gandhinagar, Gujarat 382421, India

<sup>3</sup> ITW India Pvt Limited, Welding Group, Vadodara, Gujarat 391775, India

**Fig. 1** A general circuit of the GMAW process [3–6]

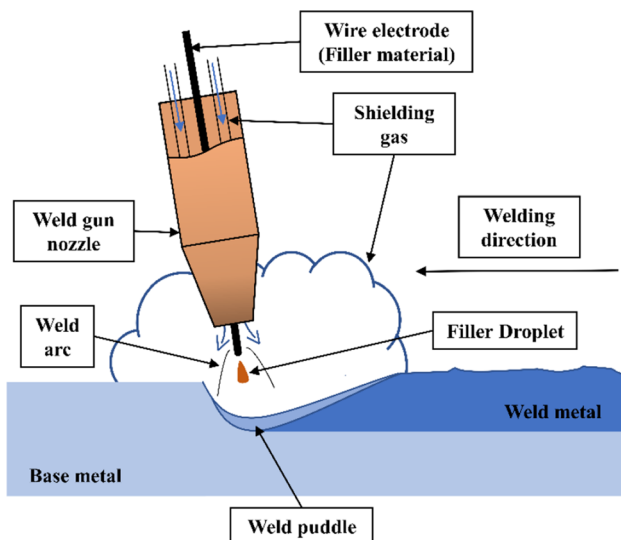
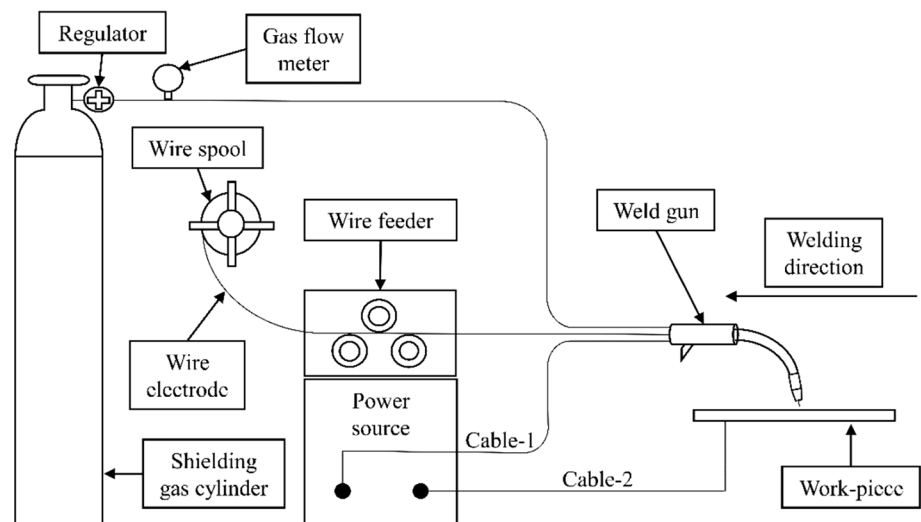


**Fig. 2** A schematic enlarged view of the welding area [3–6]

problems associated with the conventional GMAW process [1, 2, 10–15]. All these problems occur due to the occurrence of short circuits at erratic intervals which lead to the variations in the intensity of the welding arc. Because of these variations, the weld puddle agitates and yields a poor weld quality with low productivity. Unavailability of skilled personnel is the prime reason behind the inconsistency of the welding arc. When the intensity of the welding arc is low, it gives a poor depth of penetration, which further results in cold lap and cold shut, and thus, overall, incomplete fusion of materials. When the intensity of the welding arc is high, explosions in melted metal take place due to the reignition of the arc after short circuit. This leads to spattering on and around the welding beam, specifically when the inert gas used for shielding of the weld bead is carbon dioxide. Due

to spattering, extra cleaning work is required which further increases the overall time and cost of production [2, 10, 12, 13, 15].

In the era of technological evolutions, control of the weld parameter became somewhat easy due to the invention of modern welding power sources. Conventional power sources were unable to control the irregularity in weld parameters but the discovery of modern power sources completely eliminates such problems [9, 16]. These power sources consist of digital and electronic components like thermistors, transistors, inverter, etc., which enhance the accuracy and stability of the arc during the process. Since the 1990s, a modification in power sources and advancements in computer technologies have given freedom to design unlimited waveforms with the purpose of enhancing the arc timing and metal deposition. The power output regulation controls the metal transfer rate. Technological evolution brought lots of impeccable variations to the welding, specifically to GMAW, with three main categories, namely natural metal transfer, controlled transfer, and extended operating techniques. In conventional practice, the wire feed motion had been kept constant, whereas the wire speed had been adjusted with respect to the process. But now, these new advancements have synchronized both the power source and the wire feeder to attain an improved molten material transfer mode. This development has been named as mechanically assisted droplet deposition. It is extensively utilized in controlled short-circuit mode by withdrawing the wire [9, 14].

The aforesaid advancements in power source regulation have been accomplished to eliminate the drawbacks of conventional short arc waveform by designing new shapes of the arc waveform. These power sources, consisting of digital control, work on advanced software and monitor almost all characteristics of the welding arc. Furthermore, the short-circuit mode of metal transfer is predictable and

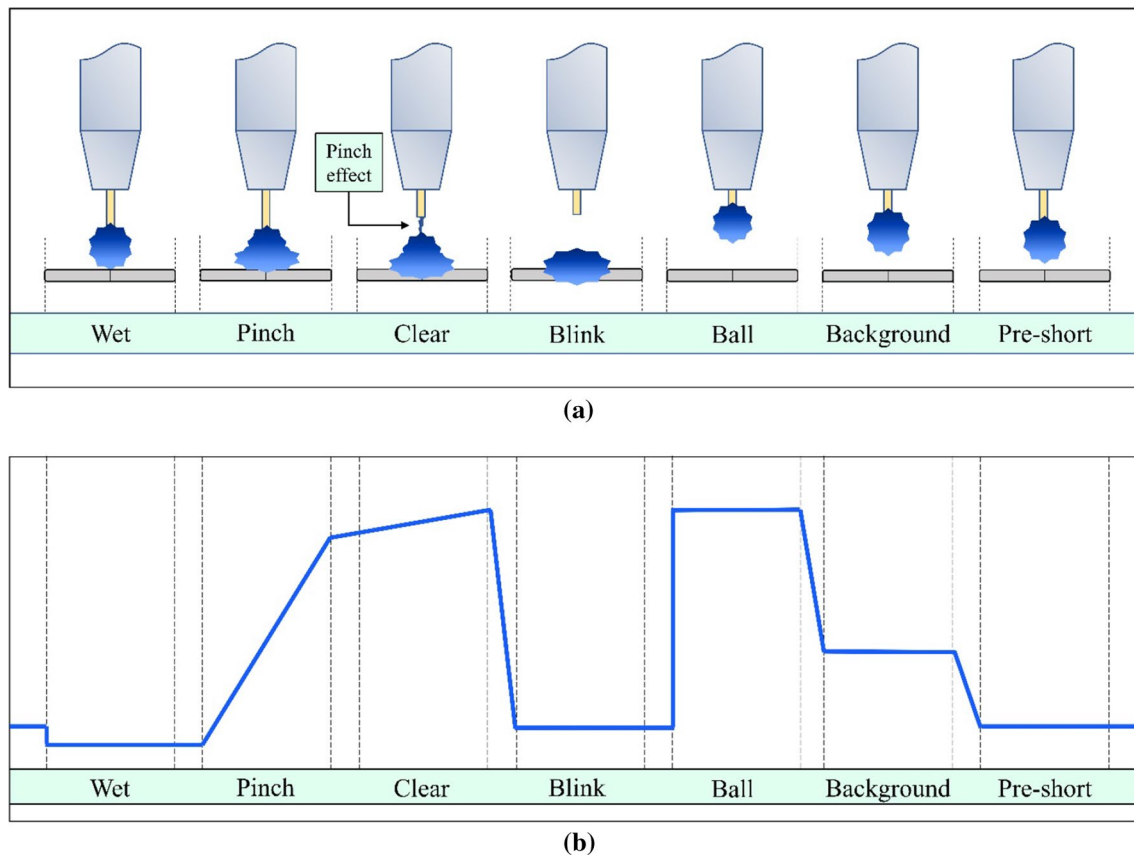


**Fig. 3** A typical RMD cycle shows **a** the distinct phases of metal transfer, and **b** the current waveform [12, 14, 19]

can be controlled at ease to reduce the spattering from the weld pool [14].

Based on the short-circuit principle of metal transfer, Miller Electric Mfg. introduced a new technique known as regulated metal deposition (RMD) welding in 2004. It is an absolutely controlled short-circuit, modified GMAW process which monitors and controls the welding current electronically amid all phases of metal transfer. It works on an advanced software application that supervises the electrode current in each progression of the short-circuiting. Because of technological advancements in power supply sources coupled with digital components and software, it predicts and regulates the short circuit and abates the welding current to make a steady metal transfer [9, 12, 14, 17, 18].

According to the manufacturer, this evolutionary technique uses a complex waveform for welding current to manipulate the short circuit. The waveform commonly relies on the thickness and the composition of the material being

welded. It consists of seven distinct phases, typically known as the RMD cycle as shown in Fig. 3 [12, 14, 19].

Nascimento and Vilarinho [20] utilized surface tension transfer (STT)—an advanced short-circuit GMAW process to join carbon steel pipes (8 mm thick and 8-in. nominal diameter) in downhill progression by means of ER70S-6 wire (1.2 mm diameter) shielded with Ar + 25%CO<sub>2</sub> gas. The welding parameters have been investigated and analyzed by performing mechanical tests and visual inspection of the samples. It was found that the advanced GMAW process yields a robust set of welding parameters with a satisfactory result. Lenin et al. [21] did root pass welding to join carbon and alloy steels by varying and controlling waveforms so that the problems like poor bridgeability and spattering could be avoided. The influence of varying waveforms on the weld bead geometry, its appearance, and soundness has also been studied along with the micro- and macro-analysis. A correlation between the process parameters and

**Table 1** Composition of ASTM 387 (11) steel

Element	Fe	C	Mn	Si	Cr	Mo	S	P
Content (%)	96.16–97.60	0.05–0.17	0.40–0.65	0.50–0.80	1.00–1.50	0.45–0.65	0.035	0.035

waveforms has been derived, and it was noticed that the average current and arc voltage amplify when the wire feed rate upsurges regardless of variation in base current. Choudhary et al. [22] performed submerged arc welding on AISI 1023 steel and investigated and optimized the weld bead characteristics using the Jaya algorithm, genetic algorithm, and desirability approach. The trails have been accomplished based on fractional factorial design, and the consequence of input parameters specifically arc voltage, welding speed, welding wire feed rate, plate thickness, nozzle to plate distance, and flux condition has been examined on different response variables like weld bead width, depth of penetration, and reinforcement. It has been observed that the welding speed is the most influencing parameter for weld bead width, whereas the penetration and reinforcement have been influenced by the wire feed rate. Ghosh et al. [23] executed metal inert gas welding and joined two dissimilar materials, namely AISI 316L austenitic stainless steel to AISI 409 ferritic stainless steel. The Taguchi orthogonal  $L_9$  array has been implemented for experimentations, and the influence of various welding parameters namely nozzle to plate distance, welding current, and gas flow rate, has been examined on yield strength and ultimate tensile strength of the welded materials. The Taguchi desirability approach has been used for discussion and analyzation of the data and also a confirmatory test has been conducted. Vedrtam and Singh [24] selected welding current, arc voltage, welding speed, and nozzle to plate distance as weld input parameters and performed submerged arc welding on stainless steel. Response surface methodology and genetic algorithm have been used for experimentation and validation of the data, and it has been found that the predicted values are similar to the experimented values. Bestard et al. [25] detailed about various technical difficulties in weld geometry calculations due to traditional sensing technologies. It has been suggested to use dynamic models, instead of static models, for better representation of the process because of the thermal inertia of welding. Lack of robustness, performance, and portability in sensory techniques is the responsible cause behind the use of flat or horizontal welding positions. It has also been observed that the vision, statistics, and artificial intelligence

**Table 2** Mechanical and thermal properties of ASTM A387 (11) steel

Properties of ASTM A387 (11) steel	
Ultimate tensile strength (MPa)	517.11–689.48
Yield strength (MPa)	310.26
Rupture strength (MPa)	37–48 (@ 575 °C)
Elastic modulus (GPa)	190–210
Brinell hardness (BHN)	180
Fatigue strength (MPa)	250
Thermal conductivity (W/m K)	39

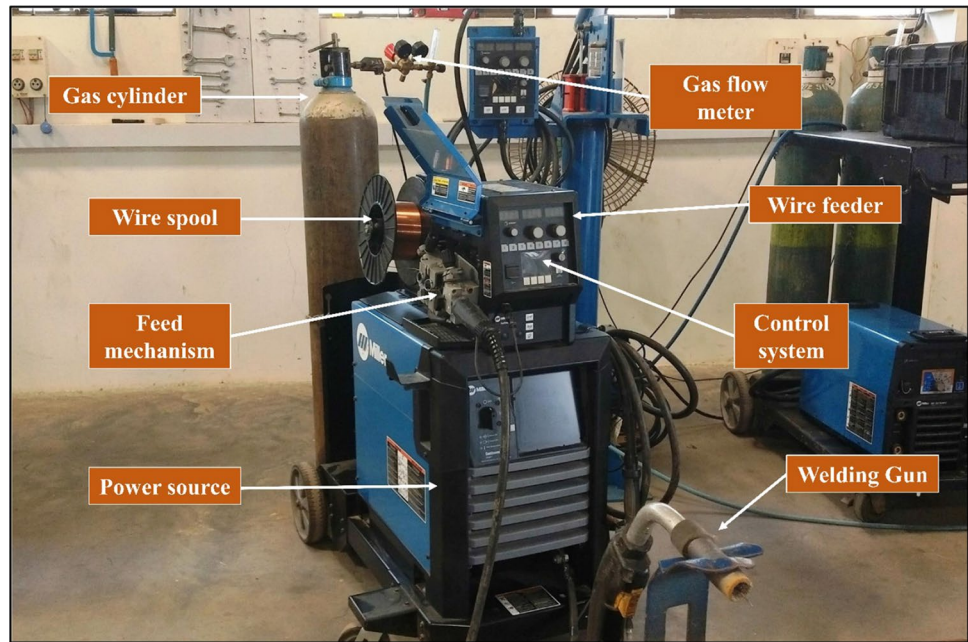
**Table 3** Weld parameters and their levels

Weld parameters	Level				
	Level 1	Level 2	Level 3	Level 4	Level 5
Weld arc current (A)	90	100	110	120	130
Weld arc voltage (V)	13	14	15	16	17
Gas flow rate (L/min)	13	15	17	19	21

(which includes artificial neural network and fuzzy inference system) are the most preferred analysis techniques for weld geometry measurement nowadays. Mastanaiah et al. [26] executed electron beam welding to join two dissimilar aluminum alloys (i.e., AA5083 and AA2219) and also studied the interaction between various process parameters and weld bead geometry. An effective weld thickness has been found the most influential weld parameter on the tensile breaking load of the material. A comprehensive metallurgical study has also been conducted to examine the other mechanical properties of the welded materials.

**Table 4** Formulation of DOE using  $L_{25}$  orthogonal array

S. no.	Current (A)	Voltage (V)	Gas flow rate (L/min)
1	90	13	13
2	90	14	15
3	90	15	17
4	90	16	19
5	90	17	21
6	100	13	15
7	100	14	17
8	100	15	19
9	100	16	21
10	100	17	13
11	110	13	17
12	110	14	19
13	110	15	21
14	110	16	13
15	110	17	15
16	120	13	19
17	120	14	21
18	120	15	13
19	120	16	15
20	120	17	17
21	130	13	21
22	130	14	13
23	130	15	15
24	130	16	17
25	130	17	19

**Fig. 4** RMD welding machine setup**Table 5** Machine setup specification

Specification of continuum 500	
Input power	Three phase
Rated welding output	500 A @ 40 V DC 100% duty cycle
Amperage range	20–600 A
Voltage range	10–44 V
Maximum open circuit voltage (OCV)	75 V

It has been noticed from the literature that lots of work have been done on submerged arc welding (SAW), gas tungsten arc welding (GTAW), GMAW, and other welding operations to evaluate their weld performance characteristics, viz. heat-affected zone, depth of penetration, weld bead geometry, etc. Various optimization techniques have also been adopted to find out the optimal settings of parameters like voltage, current, gas flow rate, etc., during the process. But with respect to the advanced GMAW processes, specifically in the area of modified short-circuit metal transfer, very little efforts have been attempted by the researchers. The works of literature from the manufacturers focus only on the machine's specifications and applications of the RMD process rather than any experimental data. Therefore, there is a scarcity of state-of-the-art on short-circuit mode of metal transfer in the GMAW process. Hence, this work attempts to evaluate the effects of voltage, current, and gas flow rate on the welding performance characteristics, viz. heat-affected zone, depth of penetration, bead width, and bead height during RMD welding.

## 2 Experimentation setup

Before commencement of the experiments, few modules, viz. selection of influencing parameters, materials to be welded, the total number of experiments to be carried out, availability of machine setup, etc., must be discussed to execute experiments in systematic and successful manners. All these modules have been discussed as follows:

### 2.1 Selection of parameters

GMAW processes are dynamic in nature and highly influenced by variations in weld parameters. Based on the formulated hypothesis, the most influenced weld parameters are weld arc current, weld arc voltage, type of shielding gas used, diameter of electrode wire, wire feed speed, and gas flow rate [2, 9, 14, 27]. Of these, three parameters, i.e., weld arc current, weld arc voltage, and gas flow rate, have been chosen for this study.

### 2.2 Selection of base materials

In this work, Cr–Mo Grade 11 steel has been chosen to execute the RMD welding trails. It is a low-alloy steel, commercially available as ASTM A387 or ASME SA387. The generic name of A387 grade 11 steel is 1¼ chrome. The material's composition is shown in Table 1 [28].

Because of sound mechanical and thermal properties, it finds its extensive applications in sectors like energy, petrochemicals, hydrocarbon processing, and coal conversion industries. The use of AISI A387 low-alloy steel in



**Fig. 5** Penetration profiles created by wire electrodes during the GMAW process [39]

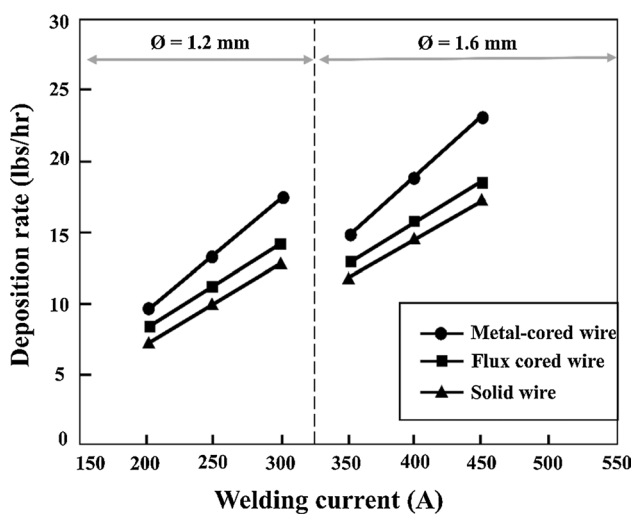
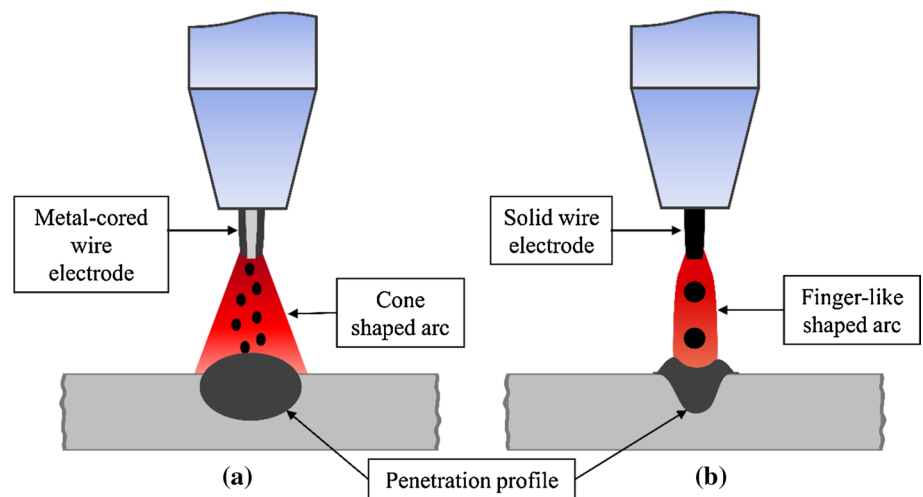


**Fig. 6** A typical comparison of deposition rates of wire electrodes [33]

aforesaid sectors is due to its proven experience at the elevated temperature of 480 °C and above. It exhibits excellent tensile strength, fatigue, and creep strength at both ambient and elevated temperature environments. It also possesses decent weldability and high hardenability due to its alloy contents. The availability of chromium (Cr) content makes the material anti-corrosive and anti-oxidant. Molybdenum (Mo) increases the strength and hardness of the material at elevated temperatures. Table 2 displays a few important mechanical and thermal properties of ASTM A387 (11) steel [28–30].

Boilers, pressure vessels, flanges, ducting, fittings, pipe supports, valves, heat exchangers, ducting and piping supports, etc., are made up of ASTM A387 Gr. 11 low-alloy steel materials. These materials are highly effective in sour gas, saltwater, and elevated temperature applications [31,

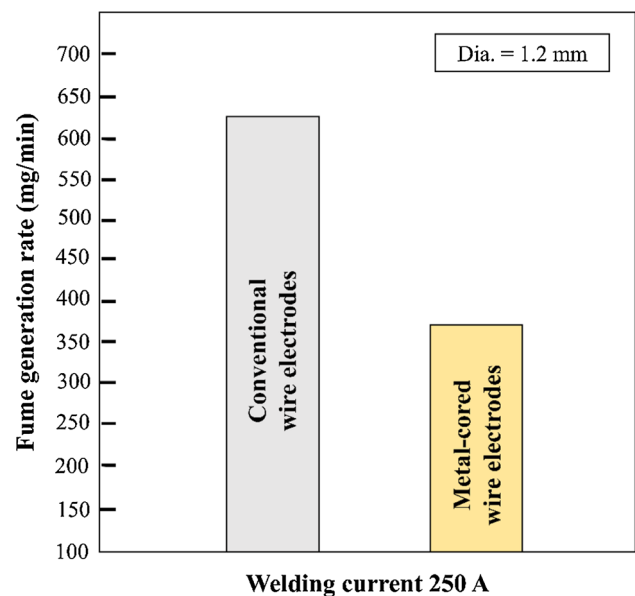


**Fig. 7** Comparison of fume generation [33]

32]. Cr–Mo low-alloy steel plates of 500 mm × 150 mm have been employed for the trail runs.

### 2.3 Parametric level setup and design of experiments (DOE)

This work investigates the impact of different weld parameters, viz. weld arc current, weld arc voltage, and gas flow rate amid RMD welding. The levels for the aforesaid weld parameters, set during the experimentation, are listed in Table 3.

An appropriate design of experiments (DOE) becomes crucial for the accomplishment of experimentation and to decide the total number of experiments to be performed as

**Fig. 8** RMD welding experimental trails on workpiece materials

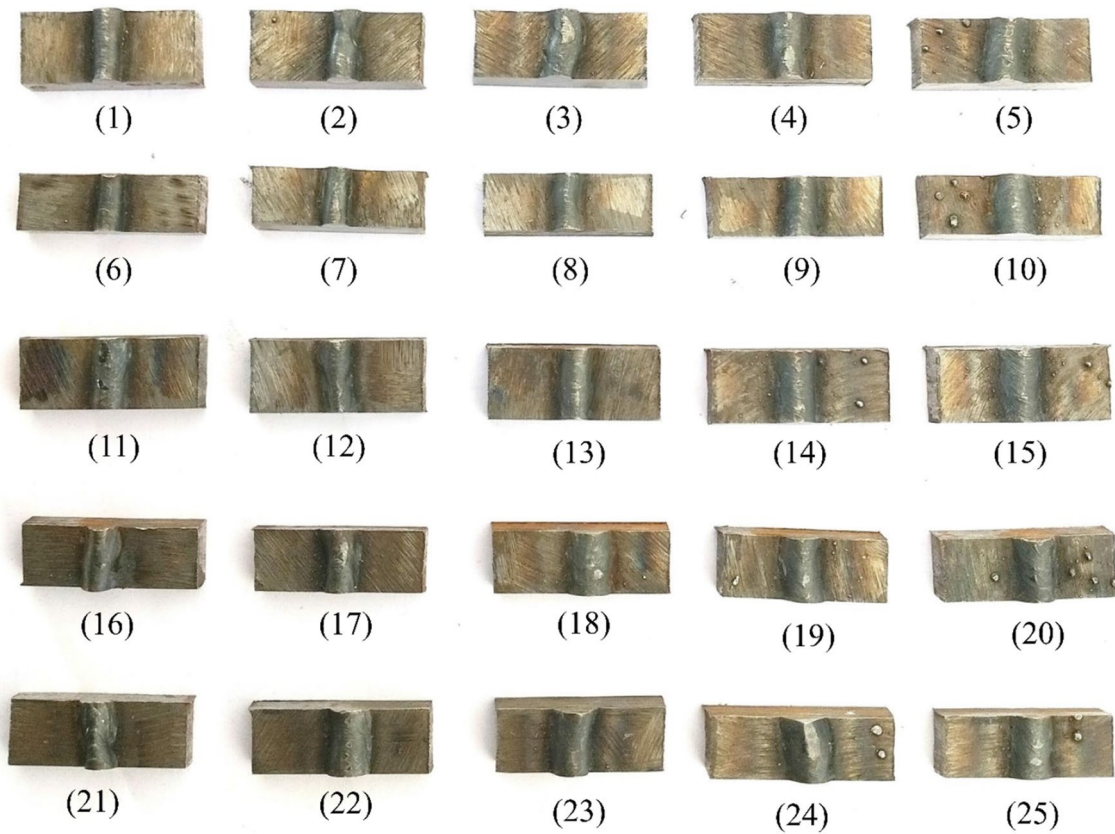


**Fig. 9** Sample specimens after the band saw cutting

**Fig. 10** MAXMEN semiautomatic horizontal band saw machine



it reduces the number of experiments which lead to saving experimental time and cost. Therefore, the concept of Taguchi's  $L_{25}$  orthogonal array has been implemented in the present study. Table 4 depicts the total number of experiments along with the level of weld parameters.

#### 2.4 Machine setup and selection of wire electrode

All the experiments, based on Taguchi  $L_{25}$  (Table 4), have been carried out on the 'Continuum 500' machine manufactured by Miller Electric Manufacturing (as shown in Fig. 4). Specifications of the machine are listed in Table 5.

Meanwhile, the selection of consumables like the wire electrode plays a very critical role in effective and economic production. The wire electrodes rapidly join two or more different materials together. Usually, three types of wire electrodes are used in arc welding processes. They are classified as the solid wire electrode, the flux-cored wire electrode, and the metal-cored wire electrode [33]. Solid wire electrodes were first introduced in 1948. These electrodes are generally made up of mild steel plated with copper. Copper plating supports electrical conductivity, stops the oxidation, and also increases the life span of the welding contact tip. They are mainly employed in the welding of thin materials like sheet metals. Though they possess high efficiency and produce nice and clean welds, some drawbacks viz. low travel speed, low deposition rate, high spatter, and requirement of cleanup after welding are associated with them [34, 35]. During the 1950s, manufacturers and fabricators were not satisfied with the performance of solid wire electrodes. Some innovative designs have been created by them to achieve higher deposition rates but most of them had flaws and were commercially unviable. Then, in 1957, a new type of wire electrode, i.e., flux-cored wire electrode, as we know it today, was introduced. The flux-cored wire electrodes are generally

preferred for thick materials. They produce strong and clean welds with low spatter level. They yield a superior depth of penetration, calm arc transfers, high material deposition rate, and are also easier to use as compared to the solid wire electrodes. Though the flux-cored wire electrodes have several benefits, they also have certain drawbacks. Sometimes, these wire electrodes result in slag inclusion or cracks in the welds which further lead to a partial fusion between the base

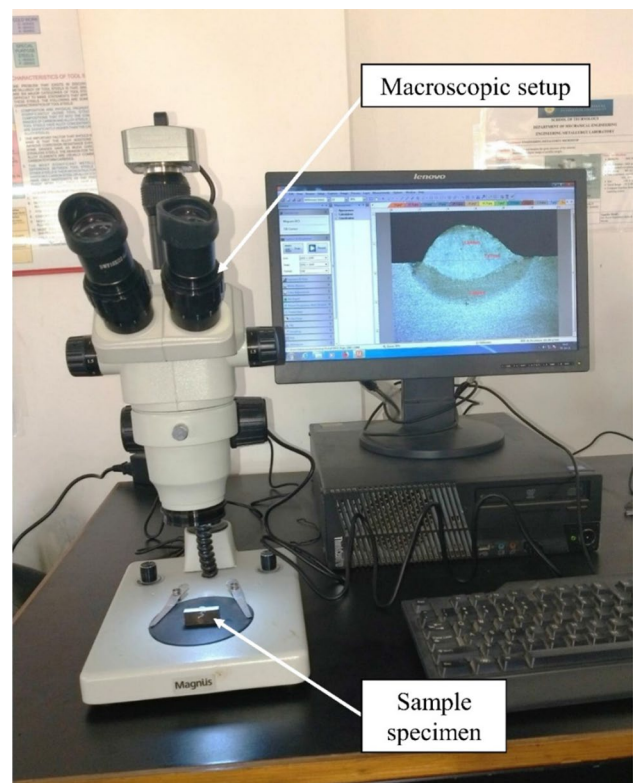


**Fig. 11** Macroscopic setup



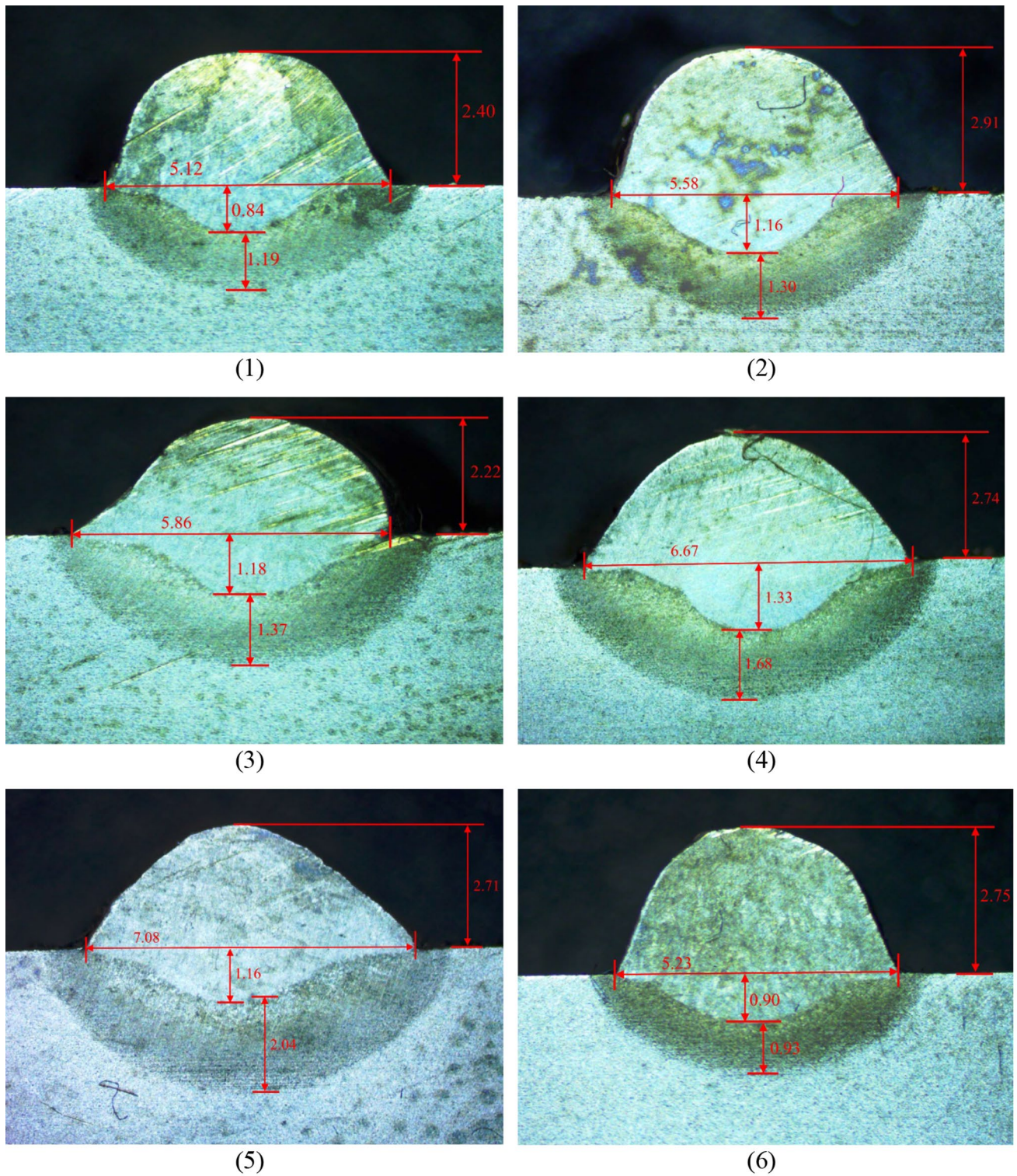
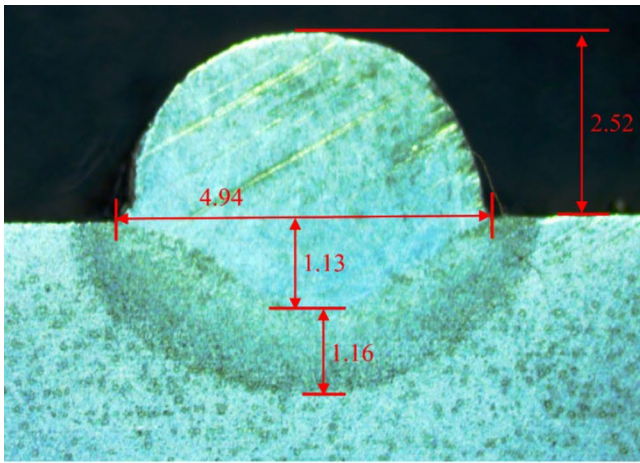
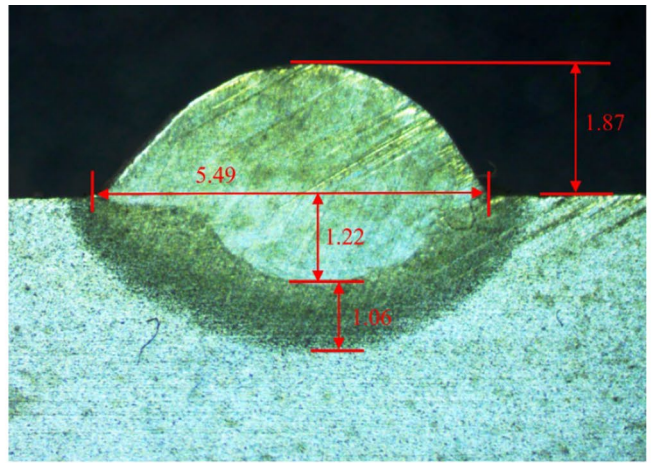


Fig. 12 Measurement of the heat-affected zone, depth of penetration, and weld bead geometry

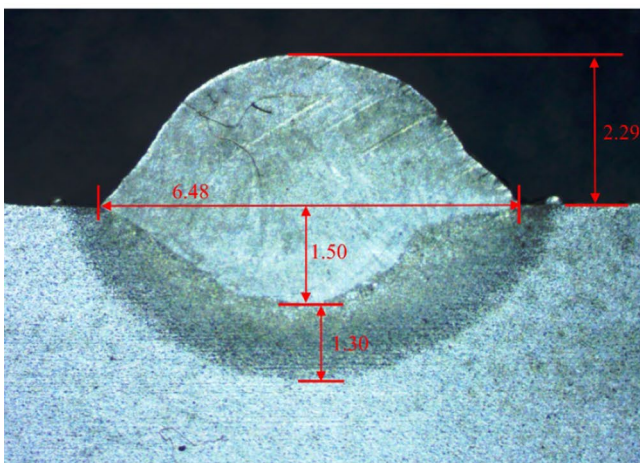




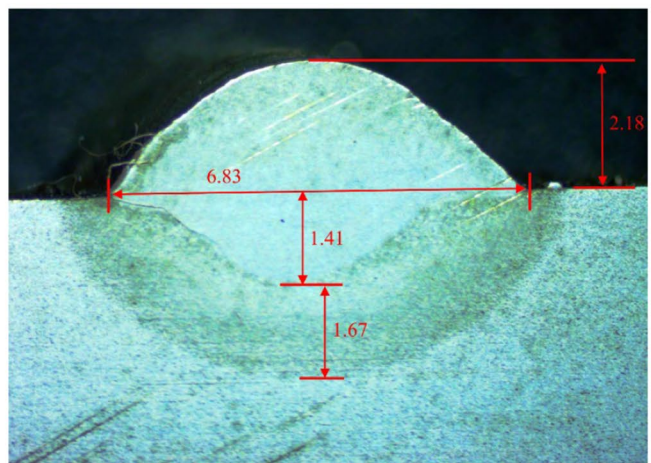
(7)



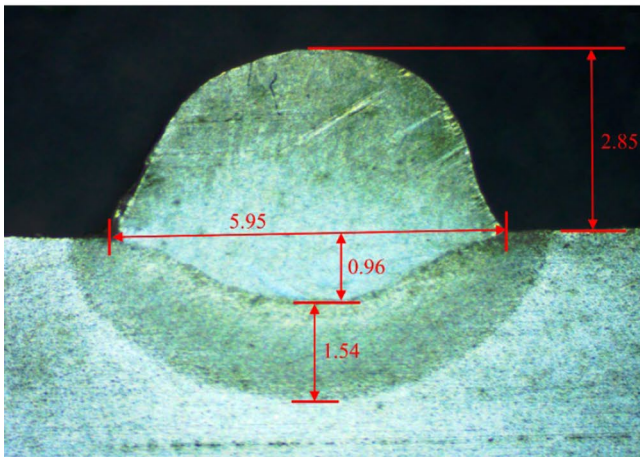
(8)



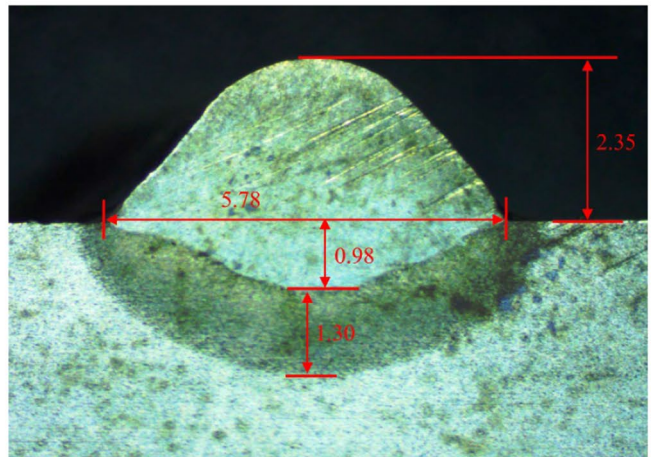
(9)



(10)



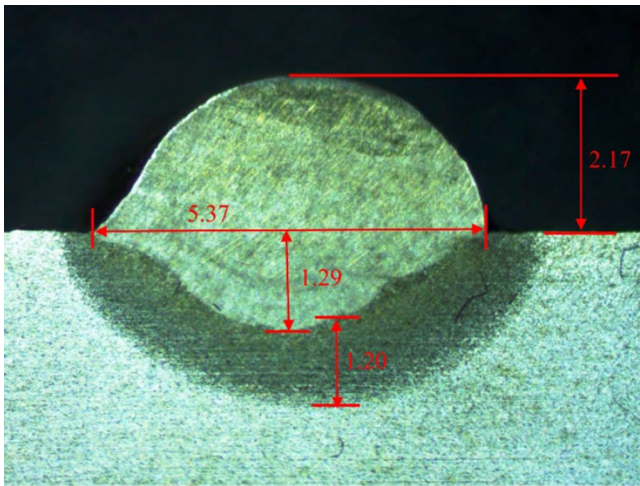
(11)



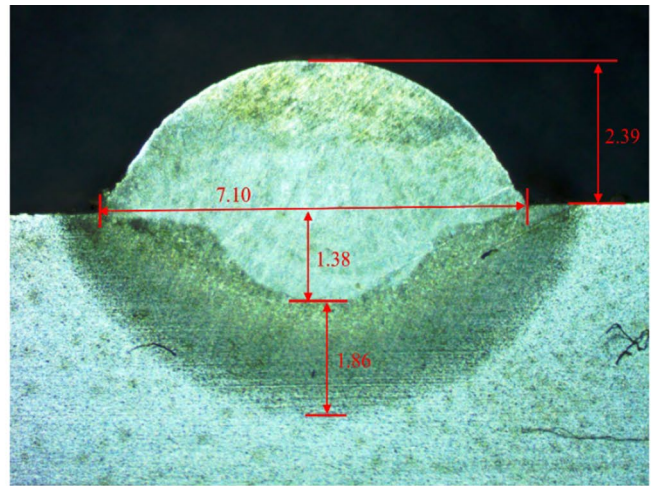
(12)

Fig. 12 (continued)

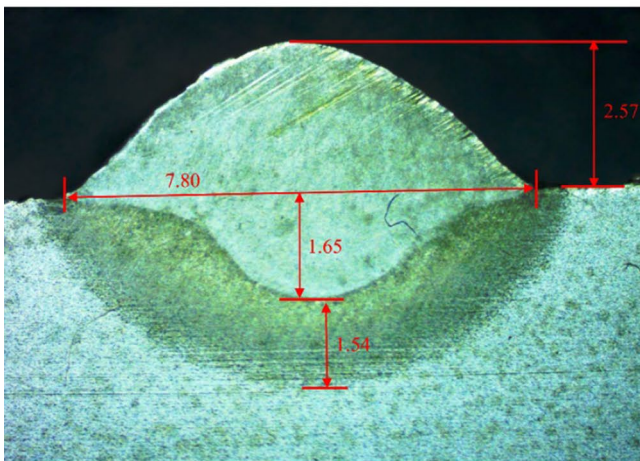




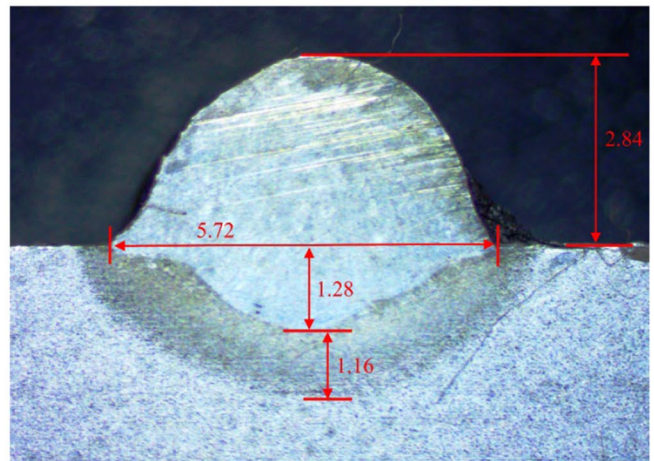
(13)



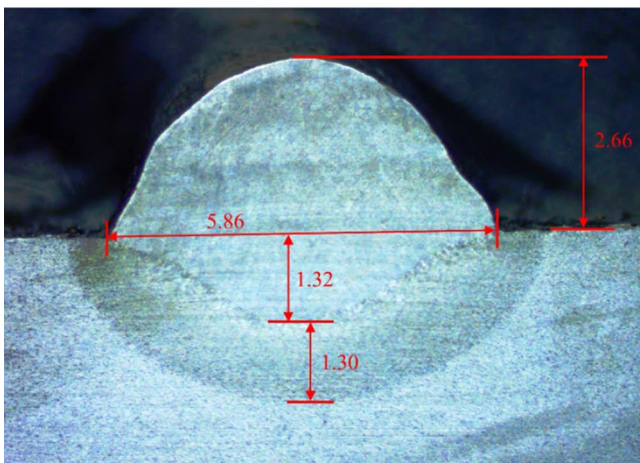
(14)



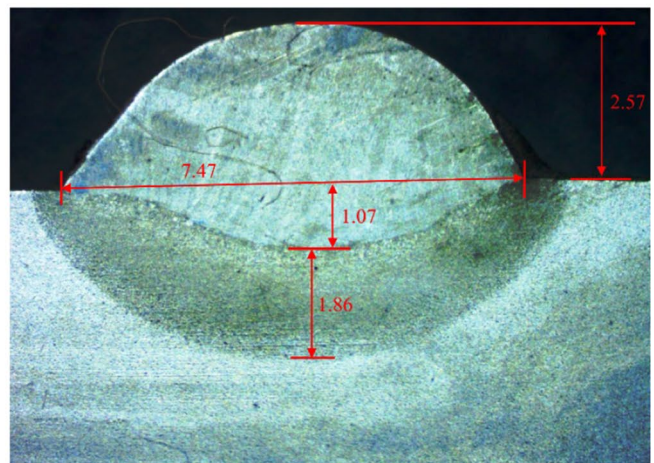
(15)



(16)



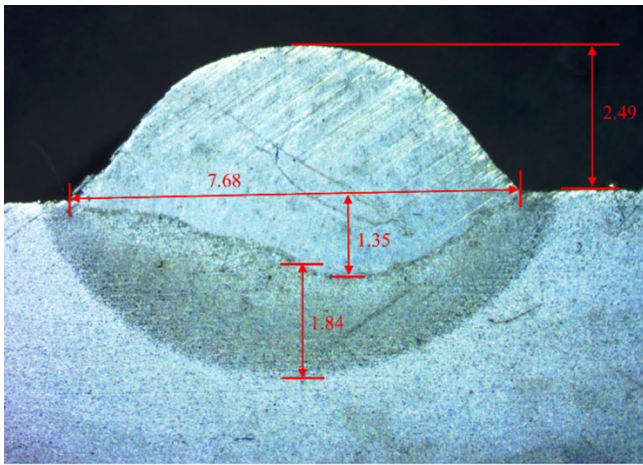
(17)



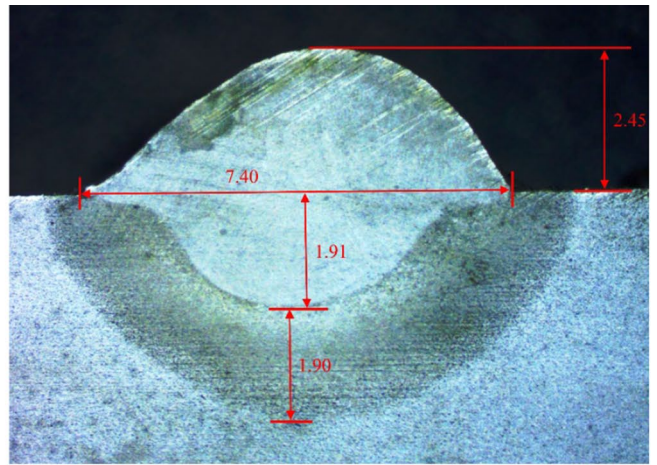
(18)

Fig. 12 (continued)

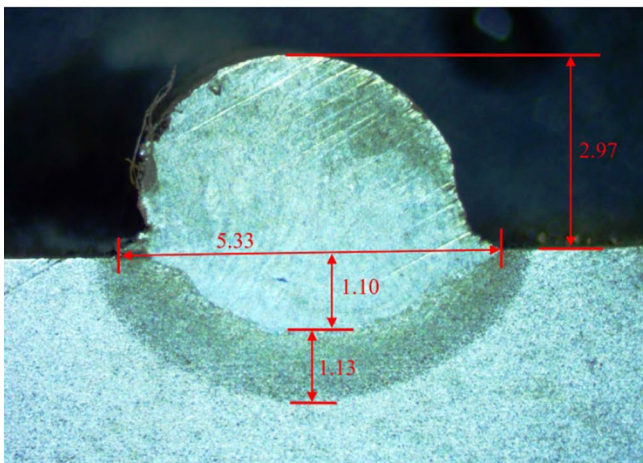




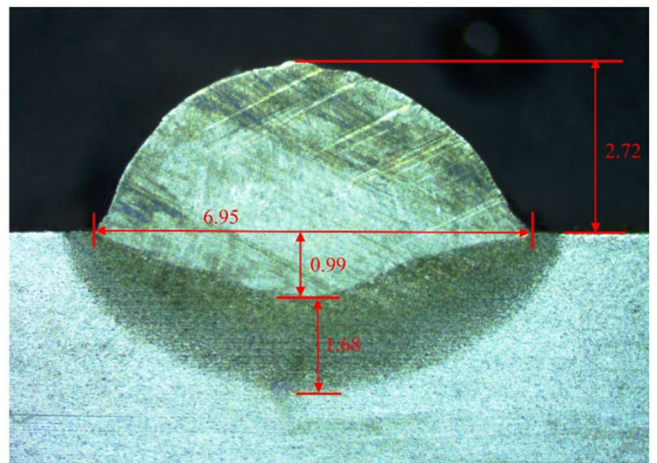
(19)



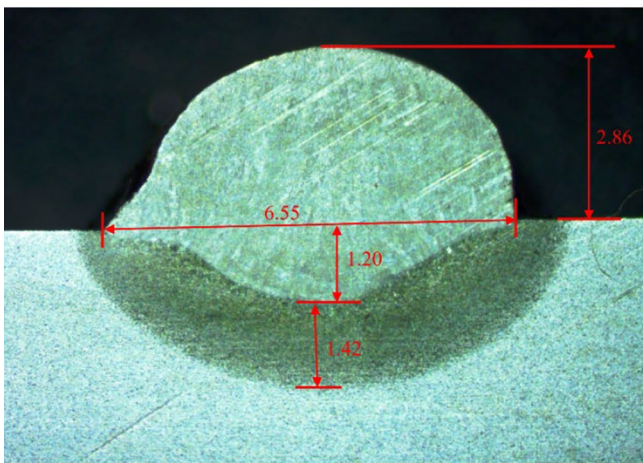
(20)



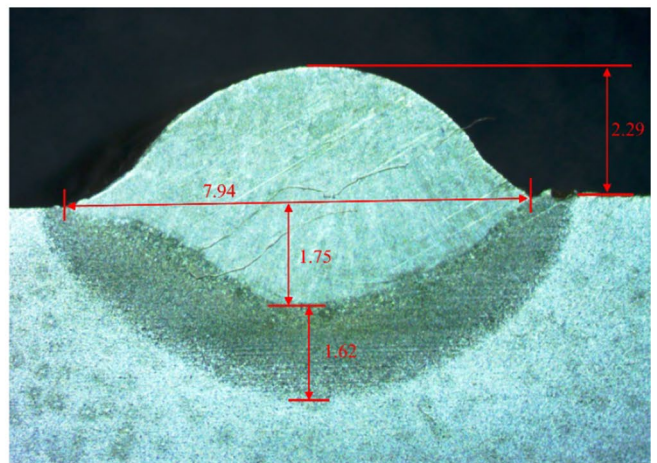
(21)



(22)



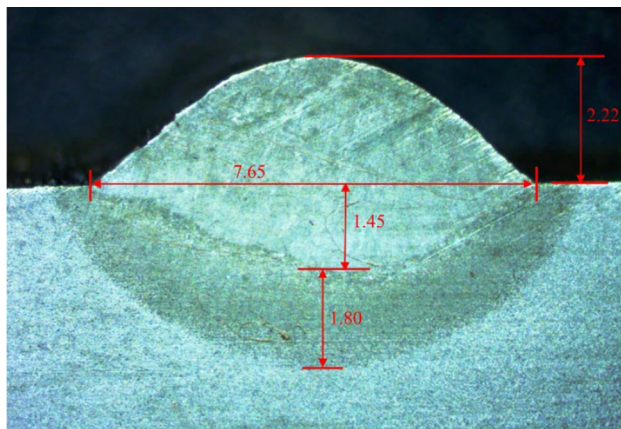
(23)



(24)

Fig. 12 (continued)





(25)

Fig. 12 (continued)

Table 6 Output response table

S. no.	HAZ (mm)	DOP (mm)	Bead width (mm)	Bead height (mm)
1	1.190	0.838	5.120	2.400
2	1.300	1.155	5.580	2.910
3	1.370	1.178	5.860	2.220
4	1.680	1.334	6.670	2.740
5	2.040	1.155	7.080	2.710
6	0.930	0.895	5.230	2.750
7	1.160	1.133	4.940	2.520
8	1.060	1.224	5.490	1.870
9	1.300	1.495	6.480	2.290
10	1.670	1.407	6.830	2.180
11	1.540	0.958	5.950	2.850
12	1.300	0.984	5.780	2.350
13	1.200	1.293	5.370	2.170
14	1.860	1.384	7.100	2.390
15	1.540	1.653	7.800	2.570
16	1.160	1.281	5.720	2.840
17	1.300	1.316	5.860	2.660
18	1.860	1.066	7.470	2.570
19	1.840	1.350	7.680	2.490
20	1.900	1.911	7.400	2.450
21	1.130	1.097	5.330	2.970
22	1.680	0.994	6.950	2.720
23	1.420	1.195	6.550	2.860
24	1.620	1.750	7.940	2.290
25	1.800	1.453	7.650	2.220

materials. The welding area may generate holes and become porous, if the gases, produced during the burning of the flux from the wire electrode, do not escape from there before the hardening of the base material. The machines and tools which use these wire electrodes are bulky and cumbersome. Due to this, they are limited to flat and horizontal positions and also not suitable for thin materials [34–36].

However, the manufacturers and fabricators were still looking for a continuous process that could be better, faster, and economical. Although their quest was about to an end with the invention of flux-cored wire electrodes, a high deposition rate was only obtained with them. The high deposition efficiencies like solid wire electrodes were yet to be achieved. The search came to an end in the form of a fabricated composite cored wire electrode, popularly known as a metal-cored wire electrode, in 1973 [34, 37]. It is a tubular-shaped hollow metallic structure loaded with a mixture of metal, minerals, and chemical powders. The powdered core materials primarily consist of iron with a diversifying quantity of alloys and arc stabilizers. Each one of these powdered core materials provides several advantages like abated oxidation, increased impact strength, and decreased silicon deposits in the final weld. These benefits make the metal-cored wire electrode as an appropriate choice for welding through mill scale. The combination of powdered core materials may vary, but usually, it depends on the filler metal manufacturers along with the desired quality, properties, and characteristics of the final weld [37–40]. These wire electrodes use high-argon (minimum 75%) CO<sub>2</sub> shielding gas mixture and are available in the diameter ranging from 0.9 to 2.4 mm. They are used in applications where single or multiple pass welding is required or applications welded in the flat, horizontal or vertical-down positions. They are well-suited for almost all varieties of steels comprising mild steels, low-alloy steels, and stainless steels. The areas of application include petrochemical, food, rail car fabrication, automobile's wheel, exhaust, and chassis fabrication, heavy equipment manufacturing, piping and other sectors where poor fit-up occurs [37, 39].

During the welding operation, the metal-cored wire electrode transmits the current through the outer metallic casing which results in a wide cone-shaped arc as shown in Fig. 5a. This arc, in turn, produces a broad penetration profile as compared to the finger-like penetration of solid wire electrodes (as shown in Fig. 5b). Due to this, a consistent bead profile is created which easily and accurately bridges gaps in the weld joints without any burn through [38, 39].

The spray transfer method is employed for the usage of metal-cored wire electrodes which produces and propels the very small droplets of filler metals into the weld puddle with minimum to no spatter generation. With this method, a very high deposition efficiency around 92–98%

**Table 7** ANOVA for HAZ

Source	<i>df</i>	Adj SS	Adj MS	<i>F</i> value	Contribution (%)	<i>P</i> value
Weld current (A)	4	0.4332	0.1083	3.37	19.11	0.046
Weld Voltage (V)	4	1.1972	0.29931	9.31	52.81	0.001
GFR (L/min)	4	0.2506	0.06265	1.95	11.05	0.167
Error	12	0.3858	0.03215		17.01	
Total	24	2.2668				

**Table 8** ANOVA for DOP

Source	<i>df</i>	Adj SS	Adj MS	<i>F</i> value	Contribution (%)	<i>P</i> value
Weld current (A)	4	0.1714	0.04284	1.51	10.51	0.262
Weld voltage (V)	4	0.9622	0.24056	8.46	59.02	0.002
GFR (L/min)	4	0.1553	0.03883	1.37	9.5	0.303
Error	12	0.3412	0.02843		20.93	
Total	24	1.6301				

**Table 9** ANOVA for BW

Source	<i>df</i>	Adj SS	Adj MS	<i>F</i> value	Contribution (%)	<i>P</i> value
Weld current (A)	4	4.485	1.1212	6.74	20.67	0.004
Weld Voltage (V)	4	13.838	3.4595	20.79	63.78	0
GFR (L/min)	4	1.376	0.344	2.07	6.34	0.148
Error	12	1.997	0.1664		9.20	
Total	24	21.696				

**Table 10** ANOVA for BH

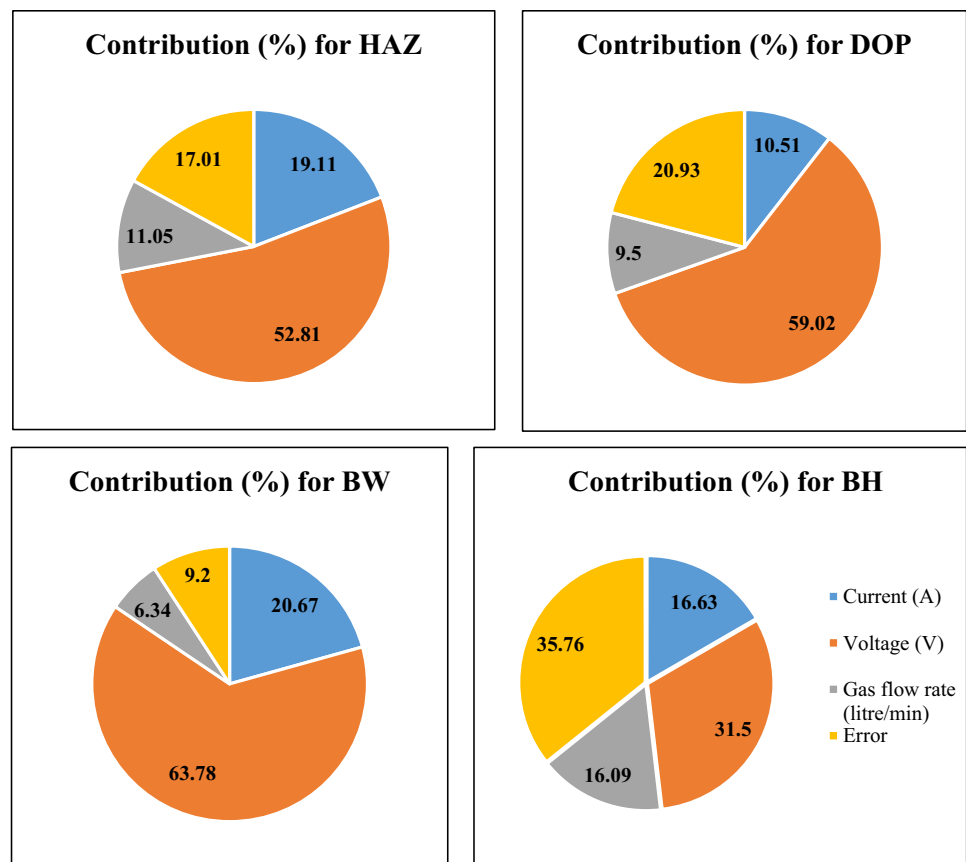
Source	<i>df</i>	Adj SS	Adj MS	<i>F</i> value	Contribution (%)	<i>P</i> value
Weld current (A)	4	0.3154	0.07885	1.4	16.63	0.294
Weld Voltage (V)	4	0.5973	0.14933	2.64	31.50	0.086
GFR (L/min)	4	0.3051	0.07626	1.35	16.09	0.308
Error	12	0.6781	0.05651		35.76	
Total	24	1.8959				

is achieved [34, 37, 39]. A metal-cored wire electrode possesses the benefits of both the solid wire electrodes and the flux-cored wire electrodes. It incorporates the high efficiencies of a solid wire electrode with the high deposition rates of a flux-cored wire electrode. Figure 6 illustrates a typical comparison of deposition rates of all three wire electrodes. A metal-cored wire electrode of 1.2 mm (0.045") diameter has a deposition rate of 12–14 lbs/h (5.4–6.4 kg/h), whereas a solid wire electrode with the same diameter has a deposition rate of 8–10 lbs/h (3.6–4.5 kg/h) [33, 34, 41]. Other benefits of metal-cored wire electrode include faster travel speeds, higher duty cycles, overcome mill scale problem, little to slag and spatter-free weld generation, reduction in weld defects such as porosity, lack of fusion, and undercut, and elimination of cleanup work and post-weld actions like grinding [33, 34, 36–40]. It has a less adverse effect on

the human operator as well as on the environment due to low fume generation as compared to the conventional wire electrodes (Fig. 7) [33].

Although the initial cost of the metal-cored wire electrode is high, all the aforementioned benefits significantly reduce the labor costs of the entire process. Hence, adopting this technology leads to better cost-effective welding with superior quality and higher productivity [33, 34].

In this context, 'MEGAFIL 237 M' metal-cored wire electrode has been chosen and used in the experimentation. To protect the weld pool from contamination, a mixture of 90% argon (Ar) and 10% carbon dioxide (CO<sub>2</sub>) gasses has been used as a shielding gas. Before the commencement of the experiments, the wire spool was set at the wire feeder which passes the wire to the hose and then feeds it to the nozzle of the weld gun. After setting up the machine, a total of 25 trails was taken on the workpiece material in a similar

**Fig. 13** Percentage contribution of parameters on responses

manner as shown in Fig. 8. Enough cooling time was provided to each trail.

## 2.5 Sample preparation

The sample preparation has to be carried out in order to analyze the influence of weld parameters which involve the cutting, etching, and polishing of the trialed workpieces. Initially, the samples have been prepared with the dimensions of 15 mm length, each side from the center of the weld bead, and 10 mm width (Fig. 9) on MAXMEN semiautomatic horizontal band saw machine (Fig. 10).

## 2.6 Macroscopic examination

The sample specimens have been polished and etched for macroscopic examination. 2% nital etch has been used as an etchant followed by water rinsing to examine the effects of weld parameters. Etched samples have been kept under the macroscopic setup (Fig. 11), and the output responses viz. heat-affected zone (HAZ), depth of penetration (DOP), and weld bead geometry (WBG) for each sample are measured as shown in Fig. 12. All the details related to the macroscopic measurements are noted down and tabulated as shown in Table 6.

## 3 Result and discussion

This section describes the effect of welding variables on the welding characteristics along with the optimization of the aforementioned characteristics.

### 3.1 Effect of welding variables on the welding characteristics

Initially, ANOVA has been applied in order to investigate the influence of the welding parameters on welding characteristics, viz. HAZ, DOP, bead width (BW), and bead height (BH). The ANOVA for the aforementioned characteristics is given in Tables 7, 8, 9, and 10, respectively. Figure 13 shows the percentage contribution of parameters on responses.

### 3.2 Proposed optimization module

This study proposed the principal component analysis integrated with Taguchi's philosophy in order to optimize the RMD welding performance characteristics on ASTM A387 (11) steel. Principal component analysis (PCA) has been carried out to eliminate response correlation and to transform correlated responses into a lesser number of uncorrelated quality indices, called major principal components (PCs). The quality loss (QL)

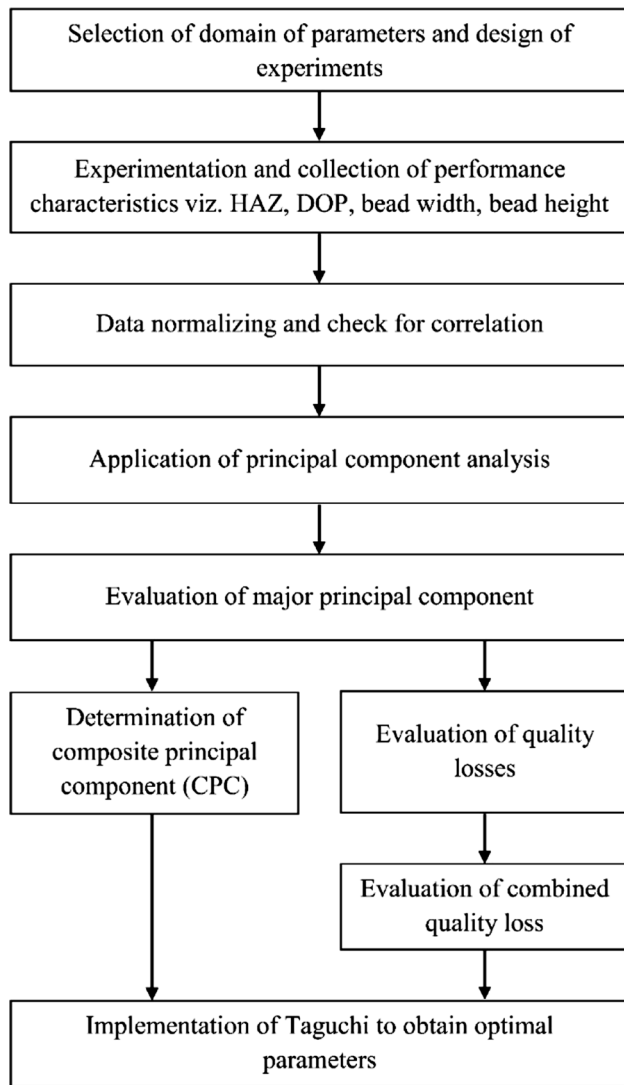


Fig. 14 Methodology adopted for the optimal solution

concept has been introduced herein representing the absolute deviation of individual PCs with respect to the ideal values. The optimal parametric setting thus obtained has been compared to that of PCA and combined quality loss (CQL)-based Taguchi optimization approaches [42]. The flowchart of aforesaid optimization approaches is shown in Fig. 14.

Initially, the experiment data, as furnished in Table 6, have been normalized and tabulated as shown in Table 11. Normalization has been essentially done to eradicate the dimensional effect and criteria conflict.

For normalizing dataset of HAZ, bead width, bead height (all correspond to lower-is-better, i.e., LB criteria), the following formula has been used.

$$Y_i^* = \frac{Y_{\min}}{Y_i} \Big|_{i=1,2,3,4,\dots,n} \quad (1)$$

Table 11 Normalized experimental data

S. no.	HAZ	DOP	Bead width	Bead height
Ideal	1	1	1	1
1.	0.781513	0.438514	0.964844	0.779167
2.	0.715385	0.604396	0.885305	0.642612
3.	0.678832	0.616431	0.843003	0.842342
4.	0.553571	0.698064	0.74063	0.682482
5.	0.455882	0.604396	0.69774	0.690037
6.	1	0.468341	0.944551	0.68
7.	0.801724	0.592883	1	0.742063
8.	0.877358	0.640502	0.899818	1
9.	0.715385	0.782313	0.762346	0.816594
10.	0.556886	0.736264	0.72328	0.857798
11.	0.603896	0.501308	0.830252	0.65614
12.	0.715385	0.514914	0.854671	0.795745
13.	0.775	0.676609	0.919926	0.861751
14.	0.5	0.724228	0.695775	0.782427
15.	0.603896	0.864992	0.633333	0.727626
16.	0.801724	0.67033	0.863636	0.658451
17.	0.715385	0.688645	0.843003	0.703008
18.	0.5	0.557823	0.661312	0.727626
19.	0.505435	0.706436	0.643229	0.751004
20.	0.489474	1	0.667568	0.763265
21.	0.823009	0.574045	0.926829	0.62963
22.	0.553571	0.520147	0.710791	0.6875
23.	0.65493	0.625327	0.754198	0.653846
24.	0.574074	0.915751	0.622166	0.816594
25.	0.516667	0.760335	0.645752	0.842342

Here,  $Y_i^*$  is the normalized data for  $i$ th experimental run ( $i = 1, 2, \dots, n$ );  $x_i$  is the experimental data for  $i$ th experimental run;  $Y_{\min}$  is the minimum value of the experimental data series.  $Y_i \mid i = 1, 2, \dots, n$ .

For the normalizing dataset of DOP (which corresponds to HB criteria), the following formula has been used.

$$Y_i^* = \frac{Y_i}{Y_{\max}} \Big|_{i=1,2,3,4,\dots,n} \quad (2)$$

Here,  $Y_i^*$  is the normalized data for  $i$ th experimental run ( $i = 1, 2, \dots, n$ );  $Y_i$  is the experimental data for  $i$ th experimental run;  $Y_{\max}$  is the maximum value of the experimental data series  $Y_i \mid i = 1, 2, \dots, n$ .

It is to be noted that after normalization, the criteria requirement of the normalized responses appears as higher-is-better (HB), and the ideal normalized data corresponds to a value unity.

Multi-objective optimization by the Taguchi method can be applied only in the case where responses are uncorrelated. Hence, a correlation test has been carried out on exploring the normalized dataset of the responses (Table 11), and the results



**Table 12** Check for correlation

Correlation between	Pearson's correlation coefficient	<i>P</i> value (probability of significance)	Remark
HAZ–DOP	−0.438	0.028	Significant
HAZ–BW	0.866	0	Significant
HAZ–BH	0.039	0.855	Nonsignificant
DOP–BW	−0.622	0.001	Significant
DOP–BH	0.284	0.169	Nonsignificant
BW–BH	−0.048	0.821	Nonsignificant

**Table 13** Results of PCA

	PC1	PC2	PC3	PC4
Eigen value	2.3183	1.1032	0.474	0.1045
Eigenvector	$\begin{bmatrix} 0.880 \\ -0.779 \\ 0.952 \\ -0.177 \end{bmatrix}$	$\begin{bmatrix} 0.305 \\ 0.326 \\ 0.16 \\ 0.937 \end{bmatrix}$	$\begin{bmatrix} 0.306 \\ 0.53 \\ 0.096 \\ -0.3 \end{bmatrix}$	$\begin{bmatrix} -0.201 \\ 0.071 \\ 0.243 \\ -0.001 \end{bmatrix}$
AP	0.58	0.276	0.119	0.026
CAP	0.58	0.855	0.974	1.000

**Table 14** Computation of major principal component (PCs) and composite principal factor

S. no.	PC1	PC2	PC3	CPL	<i>S/N</i> ratio
Ideal situation	0.876	1.728	0.632		
1.	1.1267	1.26577	0.33043	1.068911	0.578827
2.	0.8878	1.159	0.43144	0.908861	−0.83005
3.	0.7706	1.33216	0.36266	0.879784	−1.11248
4.	0.5276	1.15439	0.40572	0.690174	−3.22082
5.	0.4725	1.09428	0.3198	0.629853	−4.01521
6.	1.294	1.24597	0.4409	1.17629	1.410286
7.	1.0643	1.29312	0.43294	1.052024	0.440516
8.	0.9528	1.55737	0.39432	1.055747	0.471199
9.	0.6013	1.36035	0.46174	0.799156	−1.94737
10.	0.4532	1.32935	0.37272	0.691422	−3.20514
11.	0.8152	1.09526	0.33335	0.835651	−1.5595
12.	0.9012	1.26841	0.33514	0.936074	−0.5738
13.	0.8782	1.4116	0.42554	0.973922	−0.22952
14.	0.3997	1.23306	0.36891	0.631854	−3.98766
15.	0.3317	1.2493	0.48575	0.610278	−4.28945
16.	0.889	1.2182	0.48598	0.932981	−0.60255
17.	0.7712	1.23629	0.45392	0.864126	−1.26846
18.	0.5062	1.12195	0.29384	0.654606	−3.6804
19.	0.3739	1.19106	0.36552	0.604195	−4.37646
20.	0.1522	1.29728	0.51489	0.52059	−5.67008
21.	1.048	1.17641	0.45617	1.012096	0.104431
22.	0.6369	1.09632	0.30706	0.726714	−2.77272
23.	0.6915	1.13694	0.40808	0.782986	−2.12492
24.	0.2396	1.33832	0.47576	0.579435	−4.7399
25.	0.328	1.29805	0.37037	0.607785	−4.325

**Table 15** Computed QL corresponding to individual PCs and CQL

S. no.	QL (PC1)	QL (PC2)	QL (PC3)	CQL	<i>S/N</i> ratio
1.	0.250748	0.462229	0.30157	0.316816	9.983859
2.	0.682218	0.568999	0.200557	0.591381	4.562653
3.	0.799383	0.395844	0.269343	0.620459	4.145744
4.	1.042369	0.573606	0.226277	0.810068	1.829571
5.	1.097536	0.63372	0.312198	0.870389	1.205733
6.	0.275986	0.482033	0.191102	0.323953	9.790369
7.	0.505684	0.434881	0.199063	0.448218	6.970216
8.	0.617249	0.170631	0.23768	0.444495	7.042661
9.	0.968667	0.36765	0.170259	0.701087	3.084566
10.	1.116758	0.398646	0.259278	0.80882	1.842957
11.	0.754827	0.632741	0.298652	0.664591	3.548911
12.	0.668779	0.459586	0.296863	0.564168	4.971824
13.	0.691839	0.316402	0.20646	0.52632	5.574995
14.	1.170286	0.494944	0.263093	0.868388	1.225722
15.	1.238257	0.478705	0.14625	0.889965	1.012545
16.	0.681034	0.509797	0.146024	0.567262	4.924329
17.	0.798809	0.491711	0.178085	0.636116	3.929267
18.	1.063765	0.606054	0.338156	0.845636	1.456328
19.	1.196105	0.536937	0.266477	0.896048	0.953379
20.	1.417837	0.43072	0.117114	0.979652	0.178561
21.	0.522036	0.551588	0.175829	0.488147	6.228993
22.	0.933065	0.631679	0.324944	0.773528	2.23048
23.	0.878526	0.591064	0.223919	0.717256	2.88651
24.	1.33042	0.389678	0.156236	0.920807	0.716629
25.	1.241973	0.429952	0.261633	0.892457	0.988251

obtained are furnished in Table 12. Pearson's correlation coefficients between two response pairs (along with *p* value) are shown in Table 12. The nonzero value of the correlation coefficient of all response pairs indicates the existence of correlation to some extent.

In order to eliminate response correlation, principal component analysis (PCA) [42–45] has been carried out on the dataset given in Table 11, and the results are shown in Table 13. Table 13 shows that first, three principal components (PC1, PC2, and PC3) can take care of 58%, 27.6%, and 11.9% data variation, respectively, whereas principal component, viz. PC4, corresponds to very low accountability proportion, i.e., 2.6%.

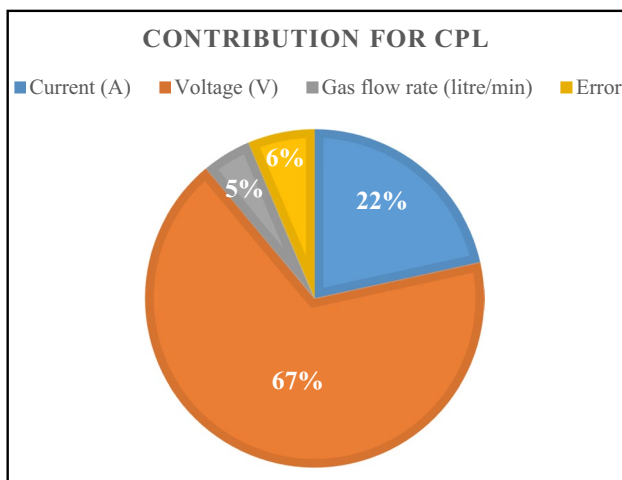
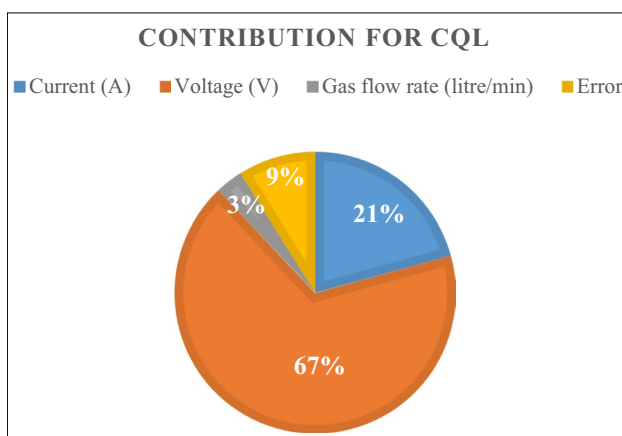
Hence, the first three principal components (PC1, PC2, PC3) have been considered as major principal components (with cumulative accountability proportion of 97.4%) and considered for further analysis. By utilizing a normalized response dataset (Table 11) and the components of the eigenvector of PC1, PC2 and PC3 obtained from PCA result (Table 13), the values of major principal components have been computed. Table 14 represents the values of individual principal components in all experimental settings including an ideal situation.

**Table 16** Analysis of variance for CPL

Source	<i>df</i>	Adj SS	Adj MS	<i>F</i> value	Contribution %	<i>P</i> value
Current	4	0.17712	0.04428	10.14	21.55	0.001
Voltage	4	0.55355	0.138388	31.68	67.36	0.000
GFR	4	0.03861	0.009653	2.21	4.69	0.129
Error	12	0.05242	0.004368		6.38	
Total	24	0.8217				

**Table 17** Analysis of variance for CQL

Source	<i>df</i>	Adj SS	Adj MS	<i>F</i> value	Contribution %	<i>P</i> value
Current	4	0.18529	0.046322	6.98	20.73	0.004
Voltage	4	0.60058	0.150145	22.61	67.19	0.000
GFR	4	0.02827	0.007067	1.06	3.16	0.416
Error	12	0.07968	0.00664		8.91	
Total	24	0.89381				

**Fig. 15** Percentage contribution for CPL**Fig. 16** Percentage contribution for CQL

Thus, by exploring PCA, correlated multi-response features (i.e., HAZ, DOP, bead width and bead height) have been transformed into three uncorrelated quality indices called principal components PC1, PC2, and PC3 to be utilized further in course of Taguchi-based optimization approach.

In weighted principal component analysis (WPCA) [31], accountability proportions of individual principal components are treated as priority weights, thus facilitating computation of composite principal component (CPC).

$$\text{CPC} = \text{PC}_1 \times w_1 + \text{PC}_2 \times w_2 + \text{PC}_3 \times w_3 + \dots + \text{PC}_n \times w_n \quad (3)$$

Assume that there are a total  $n$  number of principal components, and  $w_i$  is the accountability proportion (treated as priority weight) of  $i$ th principal component, i.e., PC $_i$ . Also,  $n_i = 1$  and  $w_i = 1$ .

Also,  $w_1 = 0.58$ ,  $w_2 = 0.276$ ,  $w_3 = 0.119$  are the weights (accountability proportion) of principal components (PC1, PC2, and PC3), respectively. Since no principal components (PC1–PC4) have been considered here,  $w_1 + w_2 + w_3 \neq 1$ . Thus, normalized weights have been explored to satisfy the condition as per Eq. 4.

$$w_1^N + w_2^N + w_3^N = 1 \quad (4)$$

This CPC is finally optimized (maximized) by using the Taguchi method. However, in the present data analysis, the values of PC1, PC2, and PC3 (refer to Table 14) for all experimental runs appear positive; but sometimes the value of principal components may appear negative. Hence, a difficulty arises in determining CPC. Therefore, quality loss estimates (corresponding to individual PCs) have been computed as shown in Table 15.

For example, (for run No. 1) QL (1), i.e., quality loss estimate for PC1, has been computed as the absolute value

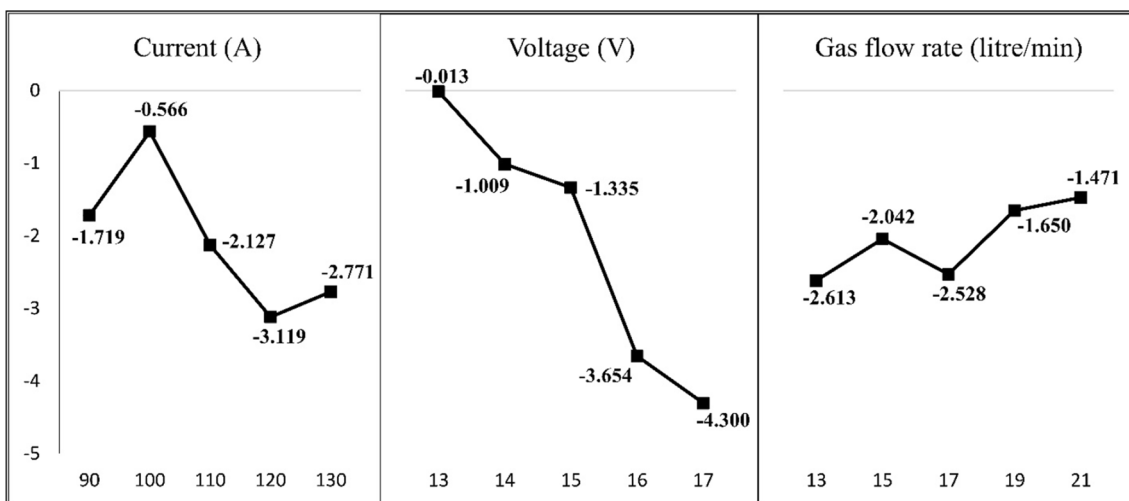


Fig. 17 Main effects plot for CPL

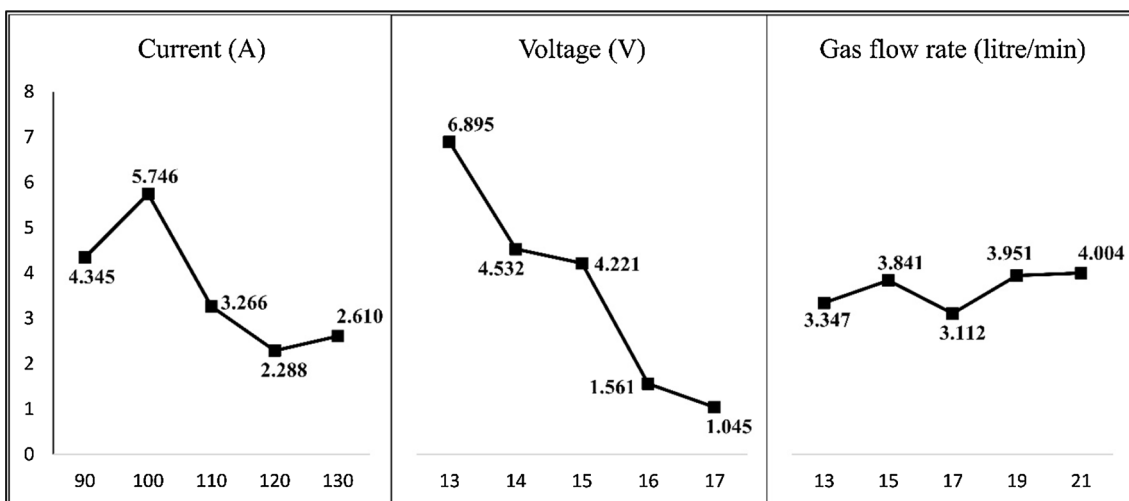


Fig. 18 Main effects plot for CQL

of the deviation of PC1 with respect to the ideal value, i.e., 10.876–1.12671. A combined quality loss (CQL) (corresponding to individual experimental runs) has been computed by aggregating quality loss estimates of individual PCs (using Eq. 5) as shown in Table 15.

$$CQL = QL_1 \times w_1 + QL_2 \times w_2 + QL_3 \times w_3 + \dots + QL_n \times w_n \tag{5}$$

ANOVA was also performed in order to investigate the influence of welding parameters on the CPL (Table 16) and CQL (Table 17). It has been observed that the voltage is the significant parameter that affects both CPL and

CQL. Figures 15 and 16 depict the percentage contribution of the welding parameters on CPL and CQL, respectively.

The optimal setting appears for both CPL and CQL as  $(I_{100}V_{13}GFR_{21})$ , i.e., current = 100 A, V = 13 V, and gas flow rate = 21 L/min. The predicted S/N ratios for CPL and CQL are shown in Figs. 17 and 18, respectively, which seem the highest as compared to the entries of S/N ratios for all experimental settings (refer to Table 14 and Table 15 for CPL and CQL, respectively). This infers that the prediction result is satisfactory. This has further been validated by a confirmatory test.

## 4 Conclusions

The foregoing research highlights an experimental investigation on the regulated metal deposition (RMD™) of low alloy steel. Conclusions drawn from the aforesaid research have been pointed out below.

1. Out of the governable welding parameters chosen in the present work (current, voltage, and gas flow rate), the voltage has a significant factor having more influence on the processes performance characteristics, viz. HAZ, DOP, bead width and bead height.
2. An efficient multi-objective optimization methodology has been proposed here by integrating PCA with the Taguchi approach. Exploration of the concept of MPCl, as well as CQL in the PCA-based multi-objective optimization module, has been demonstrated herein as an efficient optimization route for simultaneous optimization of multi-requirements of process performance yield in relation to optimize HAZ, DOP, bead width, and bead height factor in RMD welding.
3. The proposed optimization module explores the concept of maximizing MPCl as well as minimizing CQL; in both cases, the optimal setting appeared the same. This also proves validity as well as the feasibility of MPCl and CQL concepts in the PCA–Taguchi-based optimization approach.
4. The said approach can successfully be applied in any other production process (involved with multi-responses) toward continuous quality improvement as well as offline quality control.

**Acknowledgements** The authors acknowledge the efforts of ITW India Pvt Limited, Vadodara, Gujarat, and thank them for their immense support in the execution of experiments.

## References

1. MillerWelds (2017) MIG welding : the basics for mild steel. Miller Electric Mfg. LLC. <https://www.millerwelds.com/resources/article-library/mig-welding-the-basics-for-mild-steel>. Accessed 23 Mar 2019
2. MillerWelds (2018) Guidelines for gas metal arc welding (GMAW), pp 1–17
3. Kou S (2003) Welding metallurgy, 2nd edn. Wiley
4. Groover MP (2012) Fundamentals of modern manufacturing: materials, processes, and systems, 4th edn. Wiley
5. Storer J, Haynes JH (1994) The Haynes welding manual. Haynes Publishing Group, Somerset
6. Kalpakjian S, Schmid SR (2010) Manufacturing engineering and technology. Pearson Education, Inc.
7. American Welding Society. Welding fundamentals 1. <https://aws.aws.org/2014/07/i-welding-robots/>. Accessed 21 Mar 2019
8. MillerWelds (2014) Welding process training series: introduction to welding. Training Department, Miller Electric Mfg. Co
9. Das S, Vora JJ, Patel V (2019) Regulated Metal Deposition (RMD™) technique for welding applications: an advanced gas metal arc welding process. In: Advances in welding technologies for process development, pp 23–32
10. MillerWelds (2018) The most common MIG weld defects on aluminum and steel and how to avoid them. Miller Electric Mfg. LLC. <https://www.millerwelds.com/resources/article-library/the-most-common-mig-weld-defects-on-aluminum-and-steel-and-how-to-avoid-them>. Accessed 21 Mar 2019
11. MillerWelds (2018) Welding stainless steel tube and pipe : maintaining corrosion resistance and increasing productivity. Miller Electric Mfg. LLC, Appleton
12. Cuhel J (2008) Modified GMAW for root passes: modified process improves results on stainless, carbon steel pipe. Miller Electric Manufacturing Co., Appleton
13. Nazdam DJ, Armao F, Byall L, Kotecki D, Miller D (2014) Gas Metal Arc Welding Guidelines (GMAW). The Lincoln Electric Company, pp 6–93
14. Kah P, Suoranta R, Martikainen J (2013) Advanced gas metal arc welding processes. Int J Adv Manuf Technol 67(1–4):655–674
15. Wu M, Flynn D (2018) An advanced gas metal arc welding machine design for low spatter welding. In: IEEE International Symposium on Industrial Electronics, vol 2018–June, pp 335–340
16. Ohkita S, Oikawa H (2007) Latest advances and future prospects of welding technologies
17. MillerWelds (2018) Guidelines for pipe welding. Mill. Electr. Mfg. LLC, Appleton, pp 1–27
18. Cuhel BJ, Benson D, H. B. Company (2018) Welding stainless steel tube and pipe : maintaining corrosion resistance and increasing productivity controlling sensitization with filler metals, interpass temperature control filler metal selection critical in controlling carbon levels. Mill. Electr. Mfg. LLC, Appleton, pp 1–4
19. Costa TF (2011) Influence of process parameters during the pipe welding of low-carbon steel using RMD (Regulated Metal Deposition) process. In: Proceedings of COBEM 2011; 21st Brazilian congress of mechanical engineering, Copyright © 2011 by ABCM October 24–28, 2011, Natal, RN, Brazil, pp 1–10
20. do Nascimento LA, Vilarinho LO (2018) Evaluation of GMAW processes GMAW controlled short-circuit transfer (STT) applied to mechanized girth welding. In: Congresso Nacional de Engenharia Mecânica Fortaleza/CE, 2016, no 1, pp 1–16
21. Singaravelu DL, Rajamurugan G, Devakumaran K (2018) Modified short arc gas metal arc welding process for root pass welding applications. Mater Today Proc 5:7828–7835
22. Choudhary A, Kumar M, Unune DR (2019) Experimental investigation and optimization of weld bead characteristics during submerged arc welding of AISI 1023 steel. Def Technol 15(1):72–82
23. Ghosh N, Pal PK, Nandi G (2017) GMAW dissimilar welding of AISI 409 ferritic stainless steel to AISI 316L austenitic stainless steel by using AISI 308 filler wire. Eng Sci Technol Int J 20(4):1334–1341
24. Vedrtnam A, Singh G, Kumar A (2018) Optimizing submerged arc welding using response surface methodology, regression analysis, and genetic algorithm. Def Technol 14(3):204–212
25. Bestard GA, Alfaro SCA (2018) Measurement and estimation of the weld bead geometry in arc welding processes: the last 50 years of development. J Braz Soc Mech Sci Eng 40(9):444
26. Mastanaiah P, Sharma A, Reddy GM (2018) Process parameters-weld bead geometry interactions and their influence on mechanical properties: a case of dissimilar aluminum alloy electron beam welds. Def Technol 14(2):137–150



27. Costa TF (2011) Application of MAG processes with short-circuit transfer in conventional and controlled modes for carbon-steel pipe welding
28. Wilson AD, Roper CR, Orié KE, Fletcher FB (1992) Properties and behavior of modern A387 Cr–Mo steels. In: The American Society of Mechanical Engineers, Book No. G00674, pp 69–79
29. Materials General Review. Low Alloy Steels (2019)
30. AZoM (2012) AISI A387 Grade 11-PVQ Alloy Steel (UNS K11789). AZO Materials
31. Oakleysteel (2019) Chrome Moly steel plate to ASTM A387 and EN10028-3
32. Ekchard Steel and Alloys (2019) Low alloy steel plate, low alloy steel sheets, low alloy plates, SA 387 Grade Plate suppliers
33. Metal cored wires vs solid wire. Welding Engineers NZ (2019). <https://weldingengineers.co.nz/news/welding-assistance/metal-cored-wires-vs-solid-wire>. Accessed 23 Mar 2018
34. Myers D (2019) Advantages and disadvantages of metal cored wires. <https://www.esabna.com/us/en/education/blog/advantages-and-disadvantages-of-metal-cored-wires.cfm>. Accessed 23 Mar 2018
35. Flux-cored wire versus solid wire—what are the differences! (2019). <https://www.keenovens.com/articles/flux-core-solid-wire.html>. Accessed 23 Mar 2018
36. Mathison J (2019) Solid wire or flux cored wire. Fabricating & Metalworking. <http://www.fabricatingandmetalworking.com/2010/12/solid-wire-or-flux-cored-wire-2/>. Accessed 16 Mar 2019
37. Barhorst S (2007) Understanding metal-cored wire. FMA Communications, Inc
38. Know the basics to get the best results from metal-cored wire. Hobart Filler Metals (2014). <https://www.hobartbrothers.com/news/178/523/Know-the-Basics-to-Get-the-Best-Results-from-Metal-Cored-Wire.html>. Accessed 16 Mar 2019
39. How metal-cored wires reduce hidden welding costs. WIA Trusted by the best, 2019. <https://www.welding.com.au/resources-articles/view/how-metal-cored-wires-reduce-hidden-welding-costs>. Accessed 20 Mar 2019
40. Is metal cored wire the right choice. WIA Trusted by the best (2019). <https://www.welding.com.au/news/view/is-metal-cored-wire-the-right-choice>. Accessed 20 Mar 2019
41. Prajapati P, Badheka VJ (2017) Investigation on various welding consumables on properties of carbon steel material in gas metal arc welding under constant voltage mode. *Sadhana* 42(10):1751–1761
42. Routara BC, Mohanty SD, Datta S, Bandyopadhyay A, Mahapatra SS (2010) Combined quality loss (CQL) concept in WPCA-based Taguchi philosophy for optimization of multiple surface quality characteristics of UNS C34000 brass in cylindrical grinding. *Int J Adv Manuf Technol* 51(1–4):135–143
43. Abhishek K, Datta S, Mahapatra SS (2017) Multi-objective optimisation during drilling of CFRP composites: a PCA-fuzzy Taguchi integrated approach. *Int J Ind Syst Eng* 26(2):182–200
44. Abhishek K, Datta S, Mahapatra SS (2014) Optimization of thrust, torque, entry, and exist delamination factor during drilling of CFRP composites. *Int J Adv Manuf Technol* 76(1–4):401–416
45. Bijeta Nayak B, Abhishek K, Sankar Mahapatra S, Das D (2018) Application of WPCA based Taguchi method for multi-response optimization of abrasive jet machining process. *Mater Today Proc* 5(2):5138–5144

**Publisher's Note** Springer Nature remains neutral with regard to jurisdictional claims in published maps and institutional affiliations.